2012

Multipayload interferometric wave vector determination of auroral hiss

E. T. Lundberg
Cornell University

P. M. Kintner
Cornell University

S. P. Powell
Cornell University

Kristina A. Lynch
Dartmouth College, Kristina.A.Lynch@dartmouth.edu

Multipayload interferometric wave vector determination of auroral hiss

E. T. Lundberg,[1,2] P. M. Kintner,[1,3] S. P. Powell,[1] and K. A. Lynch[4]

[1]   We extend traditional, single payload, interferometric techniques to a multiple payload sounding rocket mission, and apply these techniques to measure the parallel and perpendicular wavelength of auroral VLF hiss from 8 kHz–20 kHz. We model the wavelength distribution of auroral hiss as a cone at a fixed angle with respect to the magnetic field that is isotropically distributed in the perpendicular plane. We apply this model to calculate the interferometric observables, coherency and phase, for a sounding rocket mission whose wave electric field receivers are on payloads that are separated 2–3 km along the magnetic field and 55–200 m across the magnetic field. Using an interferometer formed by comparing the collinear sphere-to-skin electric field antennas on a single payload, we estimate a lower limit on the perpendicular wavelength of VLF hiss of ∼60 m. Analysis of coherency and phase due to this conical wave vector distribution for a multipayload interferometer reveals the existence of a spin dependent coherency pattern. From this coherency pattern we generate an upper limit perpendicular wavelength estimate for VLF hiss of ∼350 m. The inter-payload phase gives an accurate estimate of the parallel wavelength of ∼6000–8000 m. This parallel wavelength is combined with the lower (upper) limit perpendicular wavelength estimates to generate upper (lower) limits on wave-normal angle. These limits are each within one degree of the predicted electrostatic whistler wave resonance cone angle verifying that VLF hiss propagates on this resonance cone.

1.   Introduction

[2]   Due to its generation via electron precipitation auroral hiss is a ubiquitous feature of the auroral ionosphere [*Maggs*, 1976]. Auroral hiss is a whistler mode plasma wave radiation that propagates in a band between the lower hybrid frequency, f_{LH}, and either the local plasma frequency, f_{pe}, or the local electron cyclotron frequency, f_{ce}, whichever is lower. The observation of enhanced wave power at f_{LH} is due to linear mode conversion from the long wavelength, propagating VLF hiss to shorter wavelength lower-hybrid waves near the lower hybrid resonance (LHR). A review of space and ground observation of auroral hiss along with applicable plasma wave theory is given by *LaBelle and Treumann* [2002].

[3]   From *in-situ* electric and magnetic field observations, *Gurnett and Frank* [1972] identified two types whistler mode wave patterns, VLF saucers and VLF hiss. VLF saucers are identified by a characteristic "saucer" shape infrequency-time spectrograms dependent on the satellite's position relative to the saucer source region. The characteristic shape is due to relatively small source regions, which can be viewed as point emitters, and the whistler waves' frequency dependent group velocity. VLF hiss, on the other hand, is generally broad-band, has a larger source region and has a Poynting vector aligned down the magnetic field.

[4]   Sounding rocket studies have been important for studying the transition from whistler mode waves to electrostatic lower hybrid waves. *Ergun et al.* [1991] used a quadrupole VLF wave receiver to measure perpendicular wavelengths of ∼12 m near f_{LH} at ∼4 kHz and up to ∼70 m at 10 kHz. These results were confirmed and extended by *Kintner et al.* [2000] who used interferometric techniques to determine that the perpendicular wavelength of VLF hiss was at least ∼80 m at 20 Khz. Due to its connection to lower hybrid waves VLF hiss is an energy source for lower hybrid solitary structures (LHSS) [*Schuck et al.*, 2003]. LHSS are gyroscale, ∼40 m wide, cylindrical, 10–50% density depletions. These density depletions may be formed and sustained by VLF hiss and lower hybrid waves scattering off of pre-existing plasma density irregularities.

[1]Department of Electrical and Computer Engineering, Cornell University, Ithaca, New York, USA.
[2]Now at MITRE Corporation, Bedford, Massachusetts, USA.
[3]Deceased 16 November 2011.
[4]Department of Physics, Dartmouth College, Hanover, New Hampshire, USA.
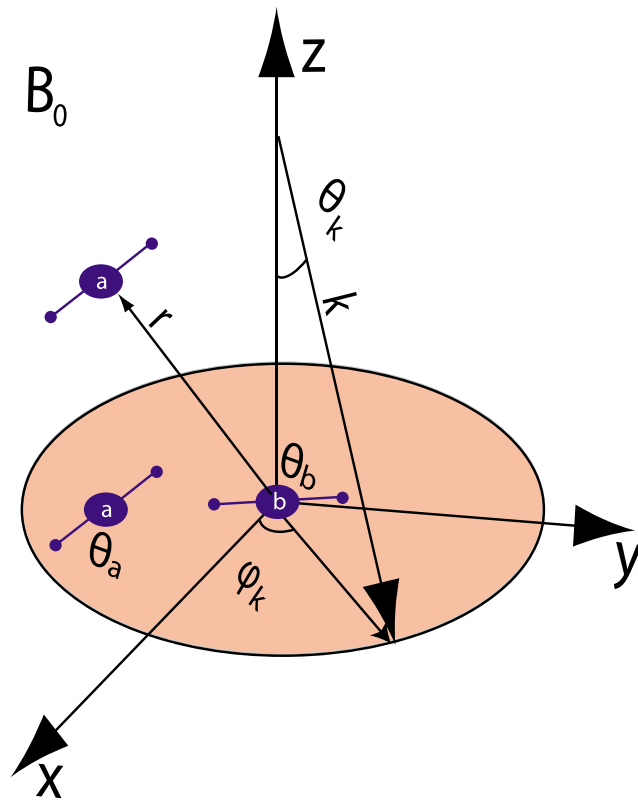
Figure 1. A diagram describing the relative positions and orientations of the payloads and the wave vector distribution. (Not to scale.)

[5] The promise of spaced measurements in space plasma is a resolution to the spatio/temporal ambiguity that plagues single point measurements. The introduction of multiple satellite missions such as CLUSTER, and multipoint measurements from a single platform on both satellites and rockets has yielded a number of techniques to solve this ambiguity. The most common technique at VLF frequencies is interferometry [*Kintner et al.*, 2000]. Two competing techniques have arisen for analysis of low frequency (DC-2Hz) plasma waves from multiple satellites; k-filtering and phase differences. The k-filtering technique (also known as the wave telescope) applies a filter bank to all available baselines which estimates the spectral power at a given wave number in a maximum likelihood sense [*Pincon and Lefeuvre*, 1992]. The phase differences method deduces the wave vector by using wavelet based interferometry to measure the phase between many different baselines [*Dudok de Wit et al.*, 1995].

[6] Using spaced *in-situ* plasma wave receivers we are able to directly measure the parallel wavelength for the first time, and bound the perpendicular wavelength of auroral hiss. Within these bounds we show that VLF hiss lies on the whistler wave resonance cone. This paper is organized in 5 sections. First we introduce the Cascades2 sounding rocket. Second we review traditional plasma wave interferometric techniques and extend them for our multipayload sounding rocket mission. Third we present the multipayload

interferometry observations. Fourth we present a discussion of the observations. In the last section we draw conclusions.

2. Experimental Setup

[7] The Cascades2 sounding rocket was launched at 11:04:00 UT on 20, March 2009 from Poker Flat Research Range outside of Fairbanks, Alaska. After powered flight, two Cornell wire-boom electric/magnetic field sub-payloads were ejected from a main payload at high velocity, 15 m/s, along their spin axes which were aligned to local magnetic field, $\mathbf{B}_0$. Onboard GPS receivers provided absolute and relative position to the $\sim$5 m level and relative timing to the $\sim$175 ns level [*Powell et al.*, 2002]. Each payload was equipped with a pair of crossed 12.14 m dipole antennas formed by 4.45 cm diameter spheres at the ends of coaxial wire booms. These four spheres and the payload skin formed 6 antennas on each payload: 2 formed by the crossed dipoles, and 4 formed by measuring the potential difference between each individual sphere and the payload skin. Each antenna was connected to at least two plasma wave receivers, one measuring from DC to 1 kHz, and one measuring from 20 Hz to 20 kHz. One sphere pair on each payload was equipped with an HF snapshot receiver that took 4096 samples at 4.8 MHz (8.53 μs of data) once every 10 ms. All data presented were taken with the VLF (20 Hz–20 kHz) plasma wave receivers. Antenna orientation was deduced post flight from a modified version of the attitude determination filter/smoother presented by *Humphreys et al.* [2005].

[8] Data presented herein were taken from 350–450 s flight time as the payload array approached and passed its $\sim$562 km apogee, which occurred 430 s into the flight. Payload positions were transformed into a magnetic Vertical, East, North coordinate system where the x-axis is anti-aligned to the geomagnetic field, the z-axis points to the magnetic pole and the y-axis completes the right handed triad. During this 150 s time period, payload a went from 2500 m to 4250 m in front of payload b, along the magnetic field. In the perpendicular plane, payload a began 20 m to the North of payload b, before payload b passed it at 379 s. By 500 s payload a was 170 m South of payload b. Payload a went from 40 to 158 m East of payload b. Figure 1 displays a cartoon of the relative payload positions, and Figures 5a and 5b show the relative payload position in the perpendicular plane and along the magnetic field, respectively. These relative motions are due to the payloads' differing orbits and the curvature of $\mathbf{B}_0$.

[9] Due to slight differences in inertia properties, the sub-payloads had slightly different spin rates such that payload a completed one extra revolution over the course of the $\sim$750 s flight. Over this time period the payloads' velocity was $\sim$1780 m/s pointing $\sim$62 degrees West of North in the plane perpendicular to $\mathbf{B}_0$. The relative positions and orientations of the payloads are sketched in Figure 1. Electron data were taken on the main payload which was situated between the two wire-boom payloads.

3. Interferometry

[10] We begin our derivation of the coherency and phase response of the Cascades2 interferometers with a discussion of the response of a dipole antenna to an electrostatic plane

wave. The dipole antenna measures the potential difference between two points in space where those points are either the electrically coupled spheres at the ends of the wire-booms or the payload's aluminium body. We convert this voltage into an electric field by dividing by the distance between the two measurement points. We consider the frequency domain representation of the electric field due to a plane wave of frequency ω, wave vector $\mathbf{k}$, and phase ϕ, $\mathbf{E}(\mathbf{x}, t) = E_0\hat{\mathbf{k}}\exp(i(\mathbf{k} \cdot \mathbf{x} + \omega t + \phi))$. The voltage measured between two points due to this wave is given by the integral form of Faraday's law, $V_{12} = \int_{\mathbf{x}_2}^{\mathbf{x}_1} \mathbf{E} \cdot d\mathbf{l}$. The position and orientation of the antenna are defined by $\mathbf{r}$ and $\mathbf{d}$, where $\mathbf{r} = (\mathbf{x}_2 + \mathbf{x}_1)/2$ and $\mathbf{d} = (\mathbf{x}_2 - \mathbf{x}_1)$. The antenna response, $s = V_{12}/|\mathbf{d}|$, and its Fourier transform are given by equations (1) and (2), respectively.

$$s(\mathbf{r}, \mathbf{d}) = E_0\hat{\mathbf{k}}\cdot\hat{\mathbf{d}} \ \text{sinc}(\mathbf{k} \cdot \mathbf{d}/2)\exp(i(\omega t + \mathbf{k} \cdot \mathbf{r} + \phi)) \quad (1)$$

$$\hat{s}(\omega) = E_0\hat{\mathbf{k}} \cdot \hat{\mathbf{d}} \ \text{sinc}(\mathbf{k} \cdot \mathbf{d}/2)\exp(i(\mathbf{k} \cdot \mathbf{r} + \phi))\delta(\omega - \omega_k) \quad (2)$$

[11] Equation (1) has three main features. First is the $\hat{\mathbf{k}}\cdot\hat{\mathbf{d}}$ term which defines the relative wave vector/antenna orientation dependence. Second is the $\text{sinc}(\mathbf{k}\cdot\mathbf{d}/2)$ term which describes the antenna attenuation at wavelengths shorter than the antenna (note that $\text{sinc}(x) = \sin(x)/x$). And third is the $\exp(i(\mathbf{k}\cdot\mathbf{r} + \omega t + \phi))$ term which models the propagation of the wave past the antenna. The dirac delta in equation (2) is due to the Fourier transform, and is dropped for the remainder of the article since the frequencies and wavelengths of interest aren't affected by doppler shift. Equation (1) is easily extended to wave distributions via integration or summation over a distribution.

[12] The interferometric observables, which were first introduced in the radar community by *Farley et al.* [1981], are coherency, γ^2, and phase, ψ, and are constructed from a generalized spectral product P_{ab}. This spectral product is defined as $P_{ab}(\omega) = \langle \hat{s}_a(\omega)\hat{s}_b(\omega) \rangle$, where $\hat{s}_a$ and $\hat{s}_b$ are fourier transforms of signals s_a and s_b and the braces denote an ensemble average. In practice s_a and s_b are discretely sampled time series and $\hat{s}_a$ and $\hat{s}_b$ are calculated via the fast fourier transform (FFT). Following *Bonnell* [1997] the squared coherency and phase are defined in equations (3) and (4) respectively. We neglect the effect of noise in the measurements as it was shown by *Kintner et al.* [2000] to slightly decrease the measured coherency.

$$\gamma^2(\omega) = \frac{P_{ab}(\omega)P_{ab}(\omega)^*}{P_{aa}(\omega)P_{bb}(\omega)} \quad (3)$$

$$\psi(\omega) = \tan^{-1}(\Im(P_{ab}(\omega))/\Re(P_{ab}(\omega))) \quad (4)$$

[13] The general expression for the cross-spectral product for a distribution of plane waves is given by equation (5) which places antennas a and b at positions $\mathbf{r}_a$ and $\mathbf{r}_b$, with orientations $\mathbf{d}_a$ and $\mathbf{d}_b$ and allows for arbitrary phases p and q between each realization.

$$P_{ab} = \left\langle \begin{array}{l} \int_{\mathbf{k}_p} E_0\hat{\mathbf{k}}_p \cdot \hat{\mathbf{d}}_a\text{sinc}(\mathbf{k}_p \cdot \mathbf{d}_a/2)\exp(i(\mathbf{k}_p \cdot \mathbf{r}_a + \phi_p))d\mathbf{k}_p \\ \int_{\mathbf{k}_q} E_0\hat{\mathbf{k}}_q \cdot \hat{\mathbf{d}}_b\text{sinc}(\mathbf{k}_q \cdot \mathbf{d}_b/2)\exp(-i(\mathbf{k}_q \cdot \mathbf{r}_b + \phi_q))d\mathbf{k}_q \end{array} \right\rangle \quad (5)$$

[14] We model the quasi-electrostatic VLF-hiss waves as a cone in wave vector space as shown in Figure 1. This cone is defined by a single wave number k at a fixed zenith angle θ_k with respect to $\mathbf{B}_0$, an azimuthal angle φ_k and a random phase such that $\mathbf{k} = k[\sin(\theta_k)\cos(\varphi_k), \sin(\theta_k)\sin(\varphi_k), \cos(\theta_k)] = [k_\perp\cos(\varphi_k), k_\perp\sin(\varphi_k), k_{||}]$. The random phase imposes a filter condition inside the expectation which reduces the summation over a double integral in equation (5) to a single integral over $\mathbf{k}$ as shown in equation (6).

$$P_{ab} = E_0^2\int_{\mathbf{k}} (\hat{\mathbf{k}} \cdot \hat{\mathbf{d}}_a)(\hat{\mathbf{k}} \cdot \hat{\mathbf{d}}_b)\text{sinc}(\mathbf{k} \cdot \mathbf{d}_a/2)\text{sinc}(\mathbf{k} \cdot \mathbf{d}_b/2)$$
$$\exp(i(\mathbf{k} \cdot (\mathbf{r}_a - \mathbf{r}_b)))d\mathbf{k} \quad (6)$$

[15] The Cascades2 experiment has a number of VLF wave antennas/recievers with which to construct interferometers. We begin our investigation of equation (6) by calculating the power spectral density, P_{aa}, which will be similar for all antennas due to their orientation perpendicular to $\mathbf{B}_0$. The antennas' orientation perpendicular to $\mathbf{B}_0$ reduces the integral over $\mathbf{k}$ to an integral over φ_k. Since $\mathbf{k}$ is isotropically distributed in the plane perpendicular to $\mathbf{B}_0$ we can arbitrarily align $\mathbf{d}_a$ along the x-axis without loss of generality. Equation (6) becomes

$$P_{aa} = \left|\frac{2E_0}{kd}\right|^2 \int_0^{2\pi} \sin^2\left(\frac{kd}{2}\cos(\varphi_k)\right)d\varphi_k = \left(\frac{2E_0}{kd}\right)^2 \pi(1 - J_0(kd)) \quad (7)$$

where J_0 is the Bessel function of the first kind of order zero.

[16] As mentioned above, each payload has six VLF wave antennas, the two crossed dipoles and each individual sphere to the payload skin. We calculate P_{ab} for two of the possible single payload interferometers: 1) collinear sphere-to-skin channels, and 2) the crossed dipoles. The coherency response for an interferometer formed by comparing collinear sphere-to-skin antennas was originally calculated numerically by *Kintner et al.* [2000]. We simplify equation (6) for this interferometer by aligning it along the x-axis such that $\mathbf{d}_a = \mathbf{d}_b = [d; 0; 0]$ and $\mathbf{r}_a = [r; 0; 0]$, $\mathbf{r}_b = [0; 0; 0]$ which is solved analytically. The cross spectral product is then given by

$$P_{ab} = E_0^2\left(\frac{2}{kd}\right)^2 \int_0^{2\pi} \sin^2(kd/2\cos(\varphi_k))\exp(ikr\cos(\varphi_k))d\varphi_k$$
$$= \frac{2\pi E_0^2}{(kd)^2}(2J_0(kr) - J_0(k(r - d)) - J_0(k(d + r))). \quad (8)$$

[17] To calculate coherency for this single payload interferometer we insert equations (8) and (7) into (3)

$$\gamma^2 = \frac{(2J_0(kr) - J_0(k(r - d)) - J_0(k(d + r)))^2}{4(1 - J_0(kd))^2}. \quad (9)$$

Equation (8) is always real which means that the phase for this interferometer is always equal to zero as was shown by *Kintner et al.* [2000]. We plot this coherency as a function of antenna length and antenna separation in Figure 2. Coherency near unity occurs for perpendicular wavelengths much
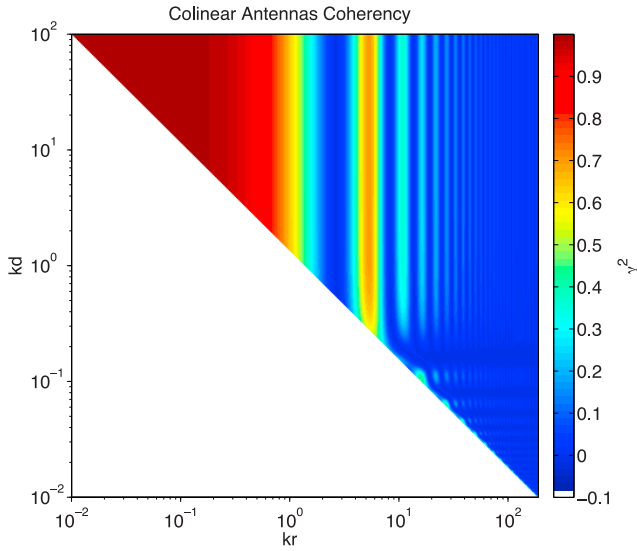
Figure 2. Coherency as a function of antenna length (y-axis) and antenna separation (x-axis) for a distribution of plane waves isotropically distributed in the plane perpendicular to $\mathbf{B}_0$. The white area is where the antenna length is longer than the separation between antennas which isn't physically realizable.

longer than the antenna separation. An interference pattern occurs for shorter wavelengths with the first null occurring at $J_0(kr) = 0$, $kr \simeq 2.404$, $\lambda = 2.612r$. We omit coherency calculation for $d >= r$ as this geometry hasn't been realized in sounding rocket applications. An approach for wavelength estimation from two collocated antennas of different lengths is presented by *Kelley and Mozer* [1972].

[18] A second single payload interferometer can be made by comparing signals from the crossed dipoles. In this case we align antenna a along the x-axis and antenna b along the y-axis such that $\mathbf{d}_a = [d; 0; 0]$, $\mathbf{d}_b = [0; d; 0]$. The cross-spectral product becomes

$$P_{ab} = \left(\frac{2E_0}{kd}\right)^2 \int_0^{2\pi} \sin\left(\frac{k_\perp d\cos(\varphi_k)}{2}\right)\sin\left(\frac{k_\perp d\sin(\varphi_k)}{2}\right)\mathrm{d}\varphi_k = 0. \quad (10)$$

This cross-spectral product of 0 leads to a straight forward interpretation of the coherency of 0. In theory we cannot calculate the phase for this interferometer due to the division operation in equation (4). In practice measurement noise will always give P_{ab} a finite length in the complex plane which leads to a measured phase.

[19] For multipayload interferometers, arbitrary antenna orientations complicate the integral in equation (6) by introducing an absolute orientation dependence, i.e., the cross spectral product depends on the antenna orientations with respect to each other and with respect to the inter-payload separation vector. To simplify, we place payload b at the origin and define payload a's position in cartesian coordinates, $\mathbf{r}_a = [r_x; r_y; r_\parallel]$. The antenna orientations in the plane perpendicular to $\mathbf{B}_0$ are defined by the angles θ_a and θ_b

measured from the x-axis. The expression for the cross-spectral product becomes

$$P_{ab} = \frac{4E_0^2}{|k|^2|d|^2}\exp(ik_\parallel r_\parallel) * \int_0^{2\pi} \sin(\mathbf{k}\cdot\mathbf{d}_a/2)\sin(\mathbf{k}\cdot\mathbf{d}_b/2)$$

$$* \exp\big(ik_\perp\big(r_x\cos(\varphi_k) + r_y\sin(\varphi_k)\big)\big)\mathrm{d}\varphi_k. \quad (11)$$

By utilizing sum-to-product trigonometric identities in the antenna orientation terms, $\mathbf{k}\cdot\mathbf{d}_{a,b}$, can be rewritten as $k_\perp d\cos(\varphi_k - \theta_{a,b})$, which makes their φ_k dependence explicit. The evaluation of this integral is complicated by these sine of cosine terms along with the existence of both $\sin(\varphi_k)$ and $\cos(\varphi_k)$ in the complex exponential.

[20] The integral in equation (11) is sufficiently complicated that we resort to computing it numerically. The first observation is that the integrand in equation (11) is always real which means that the only contribution to the inter-payload phase comes from the $\exp(ik_\parallel r_\parallel)$ term. When calculating the coherency, γ^2, this term gets multiplied by its conjugate which removes all $r_\parallel$ and $k_\parallel$ dependence. The coherency is then a function of the relative antenna orientations and their perpendicular separation. Figures 3a–3c display this coherency pattern for three different relative antenna angles, $\theta_b = 0.0, \pi/4, \pi/2$ while holding $\theta_a = 0$. The black circles that occur at the second zero of (9) and their significance is explained later in this paper. Figures 3d–3f show the relative antenna orientation for the coherency patterns displayed in Figures 3a–3c, respectively. We've fixed payload b at the origin, so Figures 3a–3c display the coherency that would be measured between two payloads for a second payload at position $[r_x, r_y]$ where r_x and r_y are denoted by the x and y axes of each plot. The essence of this calculation is that we will observe enhanced coherency in regions of space where both antennas detect waves. Since we've fixed θ_a these plots represent snapshots of the spatial coherency pattern for Cascades2. As the payloads spin the location of the second payload will describe a circle with nearly fixed radius around the origin. This will produce a pattern of nulls in the coherency spectrum. Since the payloads aren't rotating at the same rate the coherency and null pattern will change as a function of time.

4. Data Presentation

[21] Figure 4a displays the power spectral density from the FWD payload (payload a in Figure 1) between 20 Hz–20 kHz. Figure 4b displays electron count rate between 0–1 keV from a high time resolution electron detector on the main payload. The VLF wave power is concentrated near the lower hybrid frequency, f_{LH}, of ~5 kHz. Below f_{LH} there exist broadband, impulsive features that have been identified as lower hybrid solitary structures (LHSS) from 385 s to 475 s. Consistent with the model of VLF hiss as a whistler mode radiation generated by precipitating auroral electrons that has propagated a long distance from its source, the majority of the VLF wave power exists outside of regions of active auroral electron precipitation, which occur for 10 s around 425 s and from 475 s on.

[22] The inter-payload coherency and phase are displayed in Figures 5b and 5c, respectively. Figure 5a shows the inter-payload separation distance in the plane perpendicular
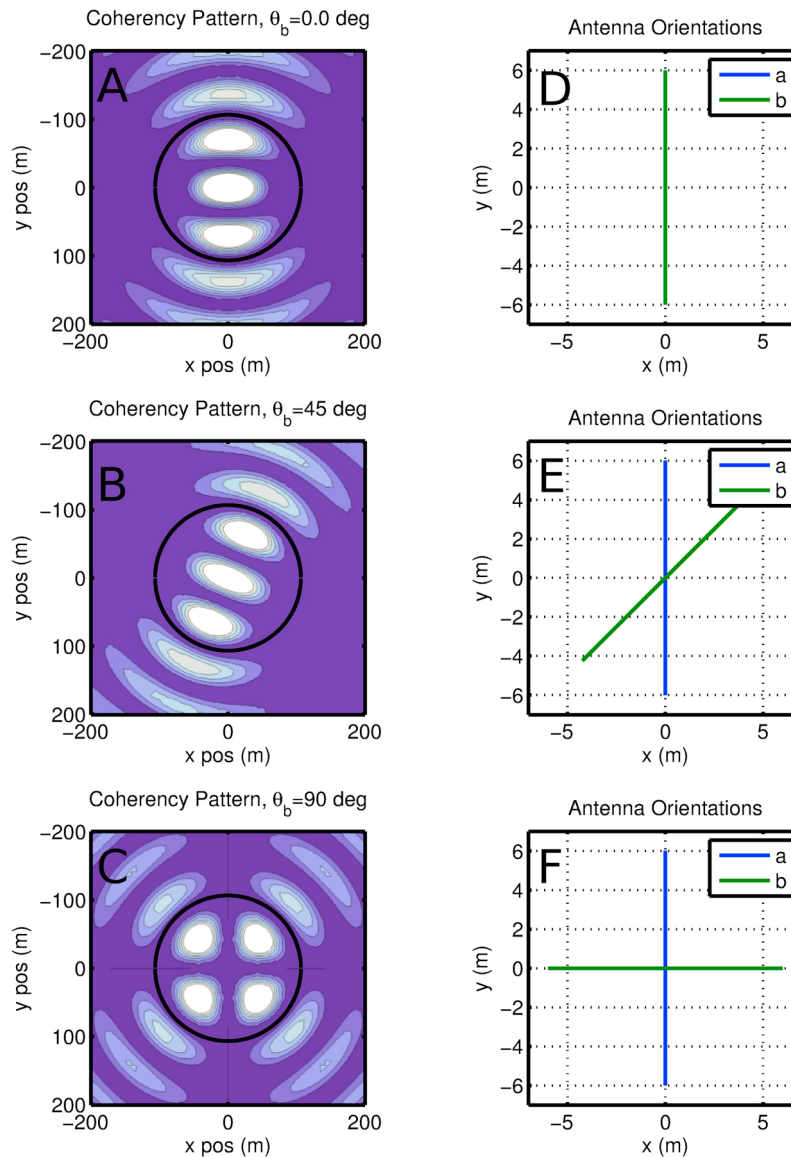
Figure 3. Coherency pattern in the plane perpendicular to $\mathbf{B}_0$ for different antenna orientations. (a–c) The coherency as a function of the interpayload separation distance for (d–f) the relative antenna orientation.

to $\mathbf{B}_0$. Figure 5d shows the separation distance parallel to $\mathbf{B}_0$ on the right axis, and the angle between the inter-payload separation vector and the IGRF derived $\mathbf{B}_0$ on the left axis. The white line in Figure 5c is the root-mean square (RMS) perpendicular separation and corresponds to the right axis.

[23] While the payloads are closely aligned along the magnetic field, and while there exists significant wave power we observe interpayload coherency near unity. As the payloads separate across the magnetic field, as a consequence of both the changing magnetic dip angle and the payloads differing orbits, the coherency decreases. Where there are coherent emissions the inter-payload phase is quite uniform changing from ∼150 degrees at 375 s to ∼180 degrees at 450 s. Note that the timing delay between payloads is at most 175 ns which would introduce a 2 degree error in the interpayload phase.

[24] We restrict our investigation of VLF hiss to the period between 375 s and 385 s because this period is relatively free of LHSS and is far from the auroral electron beam, both of which could alter the validity of our wave vector distribution model. Following *Kintner et al.* [2000] we calculate the coherency and phase for a interferometer formed by collin-ear sphere-to-skin channels on a single payload. Figure 6 displays the coherency (Figure 6a) and phase (Figure 6b) for the AFT payload (payload *b* in Figure 1). From ∼1.5–2 kHz above f_{LH} and higher the coherency is always between 0.95 and 1.0 and the phase is always within a few degrees of 0.0, indicating perpendicular wavelengths at least 10 times our antenna separation distance of 6 m isotropically distrib-uted in the plane perpendicular to $\mathbf{B}_0$. The low coherency for the ∼1.5–2 kHz above f_{LH} indicates that these lower-hybrid waves have wavelengths less than the interferometer length of 6 m.
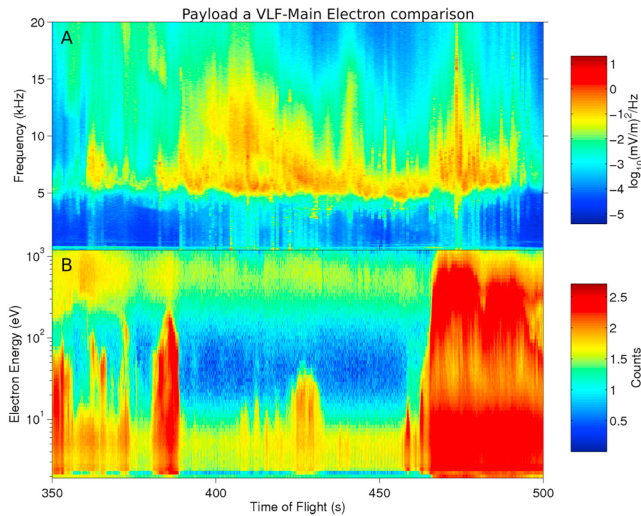
Figure 4. (a) VLF plasma wave data taken on payload a. (b) Pitch angle integrated electron count rate from the main payload.

[25] We construct a second single payload interferometer comparing signals measured from the crossed-dipole channels on the FWD payload. The coherency for this interferometer is plotted in Figure 7 and is nearly always 0.0 and is always below 0.3 for frequencies above f_{LH}. The coherent emissions below f_{LH} are due to a different wave mode and will be discussed in a future publication. The calculations leading to Figures 6 and 7 have been repeated for all similar interferometry baselines available and returned similar results.

[26] Figure 8b displays the coherency measured between the payloads. During this 10s period of the flight payload a is ~3000 m ahead of b parallel to $\mathbf{B}_0$, and the payloads are separated ~55 m in the perpendicular plane as is displayed in Figure 8a. The altitude of the payload b is ~550 km. Figure 8c displays the absolute orientation of antenna a with respect to the projection of the inter-payload separation vector into the plane perpendicular to $\mathbf{B}_0$ indicating the payloads undergo ~4 revolutions. Figure 8d displays the relative antenna orientation between the two payloads measured from payload a. The vertical black lines identify nulls
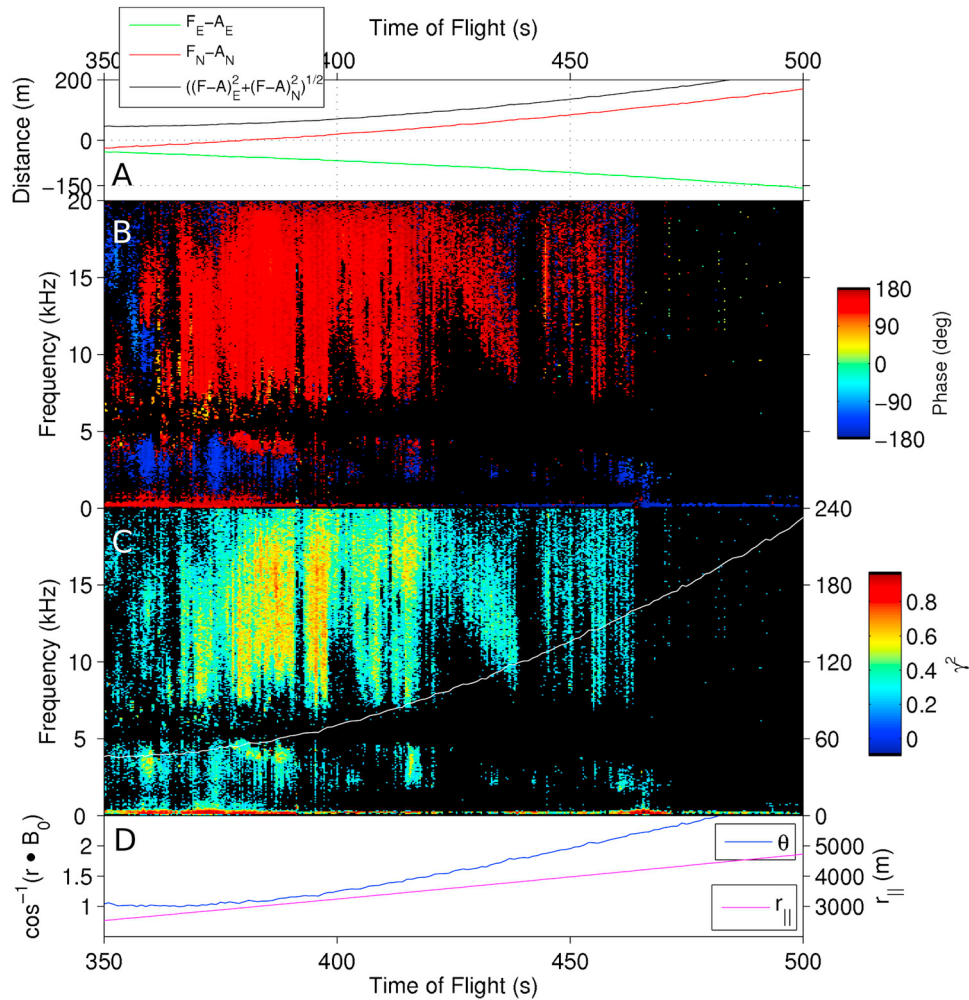
Figure 5. (a) Separation between payloads a and b in the plane perpendicular to $\mathbf{B}_0$. (b) The interpayload phase. (c) Interpayload coherency and RMS perpendicular separation (white line and right axis). (d) The angle between the interpayload separation vector and $\mathbf{B}_0$ (left axis) and the separation between payloads a and b parallel to $\mathbf{B}_0$.
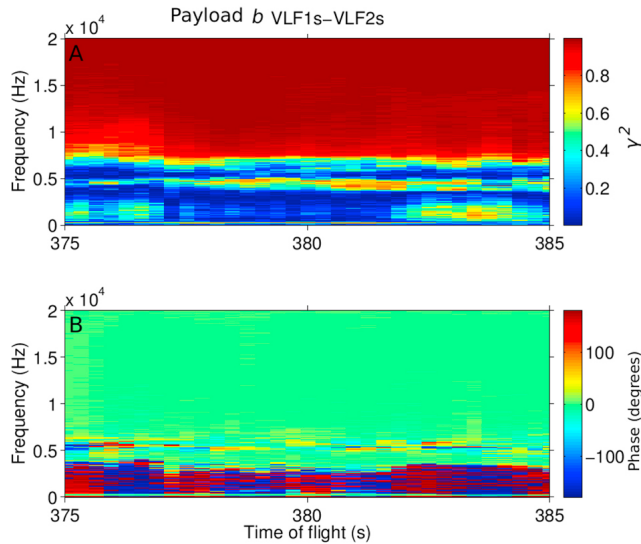
Figure 6. (a) Coherency and (b) phase from collinear sphere-to-skin channels on payload b.

in the coherency spectrum and are used in the forthcoming discussion.

5. Analysis and Discussion

[27] There are three sources of information about the perpendicular wavelength: (1) the collinear antennas on a single payload, (2) the location and depth of the nulls in the inter-payload coherency calculation, and (3) the decrease in coherency as the payloads separate across the magnetic field. As mentioned previously, the high coherency observed between two collinear antennas on a single payload (Figure 2) indicates perpendicular wavelengths at least 10 times the 6 m interferometer length.

[28] During the 10 s period displayed in Figure 8 the relative orientation of the antennas changes by $\sim$8 degrees, from -45 degrees to -53 degrees. This slight change doesn't significantly affect the coherency pattern. Figure 9 displays the theoretical coherency pattern as a function of spin for this multiple payload interferometer. The vertical lines in Figure 9 are chosen to match those of Figure 8. From the spin dependence and shallow depth of the nulls in Figure 8 we determine and upper limit of the perpendicular wavelength at $kr = 1.$, or $\lambda = 450m$.

[29] The decrease in measured coherency as a function of increasing inter-payload separation distance displayed in Figure 5 provides an *ad-hoc* estimate of the perpendicular wavelength. The first null that exists for all antenna orientations is shown in the circles in Figures 3a–3c. When x = 0, the y-axis of Figure 3a is given by equation (9). For our interferometer where $d = 12$ m and $r \sim 100$ m the first and second zeros of equation (9) occur at $k \sim .0182$, and $k \sim .052$, respectively. We could then use entrance into this null to estimate the perpendicular wavelength as either 118 m or 343 m.

[30] Since the interpayload phase is entirely due to payloads' parallel separation, ie, $k_{\parallel} r_{\parallel} = \psi + 2\pi n$ radians where $n = 0, 1, 2, 3,..$, we can use the inter-payload phase to estimate parallel wavelength. We assume $n = 0$, and solve

the expression relating $k_{\parallel}$ and ψ for the parallel wavelength, which is plotted as a function of frequency in Figure 10a. There is some evidence of phase wrap-around after $\sim$450 s which occurs when the inter-payload separation distance, $r_{\parallel}$, is equal to an integer number of half wavelengths.

[31] From the cold, two fluid plasma dispersion relation, *Maggs* [1976] derives an expression for the resonance cone-angle for VLF-hiss, $\phi_r = \tan^{-1}(k_{\perp}/k_{\parallel})$. (Note that the angle ϕ_r is the angle between **k** and **B**$_0$.) The resonance cone angle is given by equation (12), where R $= \omega_{pe}/\Omega_{ce}$ is the ratio of the plasma frequency to the electron cyclotron frequency, z $= \omega/\Omega_{ce}$ is the ratio of the wave frequency to the electron cyclotron frequency, and ξ is the electron to ion mass ratio. We've measured f$_{pe}$ to be approximately 1.2 MHz (indicating an electron density of $1.5 \times 10^4 cm^{-3}$), and calculated f$_{ce}$ to be 1.26 MHz from the IGRF magnetic field model.

$$\cos^2(\phi_r) = \left(\frac{1 + R}{R}\right)z - (1 - z)\xi - z^2/R \qquad (12)$$

Applying the ratio of our lower (upper) limit perpendicular wavelengths estimates to our directly measured parallel wavelength estimate, we obtain upper (lower) bounds on the observed VLF hiss wave-normal angle. These bounds, along with the theoretical resonance cone angle, are plotted as a function of frequency in Figure 10b. We note both the expression for ϕ_r and our interferometric observations refer to the phase-velocity resonance cone. For whistler waves propagating near the resonance cone the group velocity is perpendicular to the phase velocity forming a group velocity cone whose angle is the complement of the phase velocity cone [*Fisher and Gould*, 1971]. It is this group velocity cone that is observed in VLF saucers. From our phase velocity cone angle measurements we deduce the group velocity (power flow) of VLF hiss waves to be between 0.5 and 2.0 degrees with respect to **B**$_0$. There is some evidence of saucer structure between 375 s and 450 s in Figure 4, where the peak in the wave power above f$_{LH}$ decreases in a roughly parabolic shape.
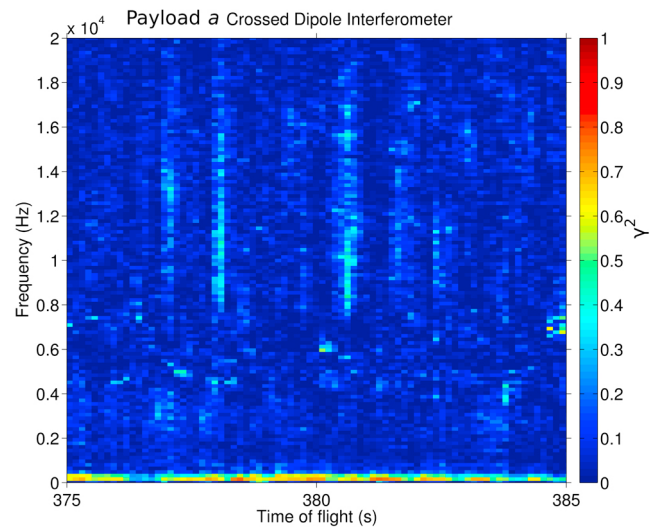
**Figure 7.** Coherency for the crossed dipole interferometer from payload a.
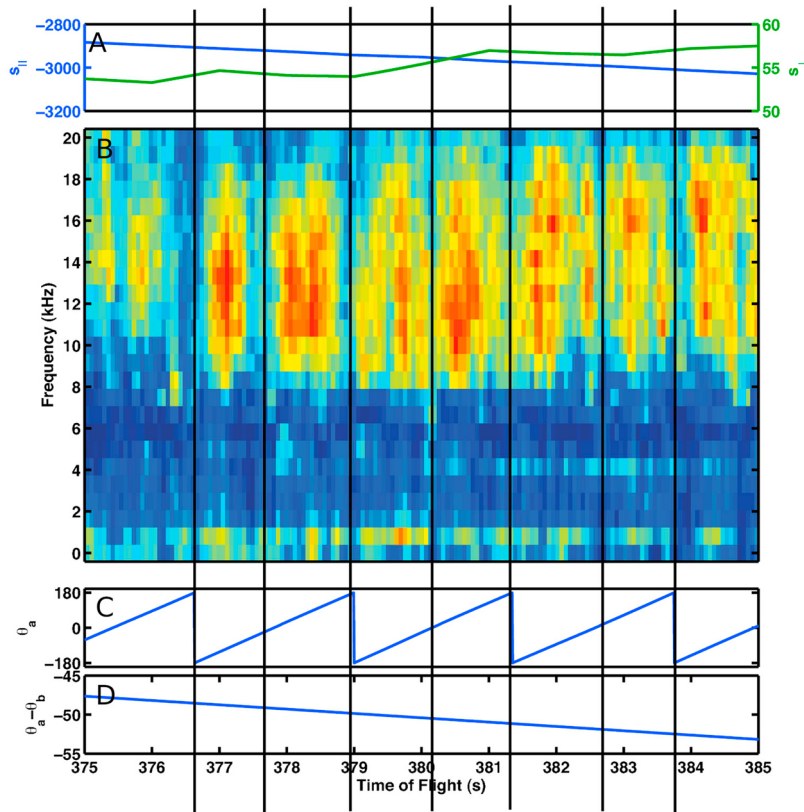
Figure 8. (a) Distance between a and b in the planes parallel (left axis) and perpendicular (right axis) to $\mathbf{B}_0$. (b) The interpayload coherency. (c) The absolute orientation of antenna a with respect to the interpayload separation vector. (d) The relative orientation of antenna b with respect to antenna a. The vertical lines identify nulls in the coherency spectrum.

[32] The predominant generation mechanism for VLF hiss has been identified as coherent beam amplification of whistlers by the auroral electron beam where these whistlers are seeded by incoherent Cherenkov radiation from the electron beam [*LaBelle and Treumann*, 2002]. The parallel wavelength is determined by the Cherenkov radiation condition, $k_\parallel = \omega/v_\phi$, where v_ϕ is the electron velocity. Figure 11a shows the calculated resonant electron velocity as a function of frequency for our measured parallel wavelengths. These energies range from 10 keV at 8 kHz to 45 keV at 20 kHz. The highest energy electron spectrograph channel was ~5 keV so we would have been unable to observe electrons with these energies. These energies are startlingly high for the aurora and can be explained a number of ways. Neither the VLF hiss nor the electrons are generated at the rocket's ~550 km altitude. The resonance calculation ignores all refraction as the VLF hiss traversed the gradual ionospheric magnetic field and electron density gradients. As pointed out by *Ergun et al.* [1991] and *LaBelle and Treumann* [2002] the parallel index of refraction generally increases as a function altitude. This means that the parallel wave number is also an increasing function of altitude, and therefore the resonant electron energy decreases as a function of altitude. A full ray-tracing code with an accurate ionospheric model could be used to remotely sense the unstable electron distribution, but this is outside the scope of this paper.

[33] A second explanation for the long observed wavelengths is that they could be due to scattering off of LHSS. One mechanism that allows VLF hiss to reach the ground is scattering by meter scale densities structures [*Sonwalkar and Harikumar*, 2000; *Ye and LaBelle*, 2008]. When VLF hiss scatters off of the density irregularities its wave vector can change from nearly perpendicular to nearly parallel, and this scattering process may also change the VLF hiss wavelength. The finite slope in inferred electron energies could mean either that there is a range of unstable electron energies, contrary to the assumptions made by *Ergun et al.* [1991], or that VLF hiss is being generated over a range of altitudes.

[34] Figure 11b shows the parallel phase velocity as a function of frequency normalized by the speed of light which is between 0.2c at 8 kHz and 0.44c at near 20 kHz. These correspond to parallel indices of refraction between 2.2 and 4.0, in close agreement of those predicted by *LaBelle and Treumann* [2002].

[35] There are two key assumptions in our model of VLF hiss as it pertains to the cold plasma dispersion relation presented above. First, the conical wave vector distribution of electrostatic waves describes both the propagation direction of the waves and their polarization. Second, the random phase approximation that was used to simplify the expression for the cross-spectral product is justified by both the isotropic perpendicular wavelength distribution of VLF hiss and by its generation via incoherent Cherenkov radiation.
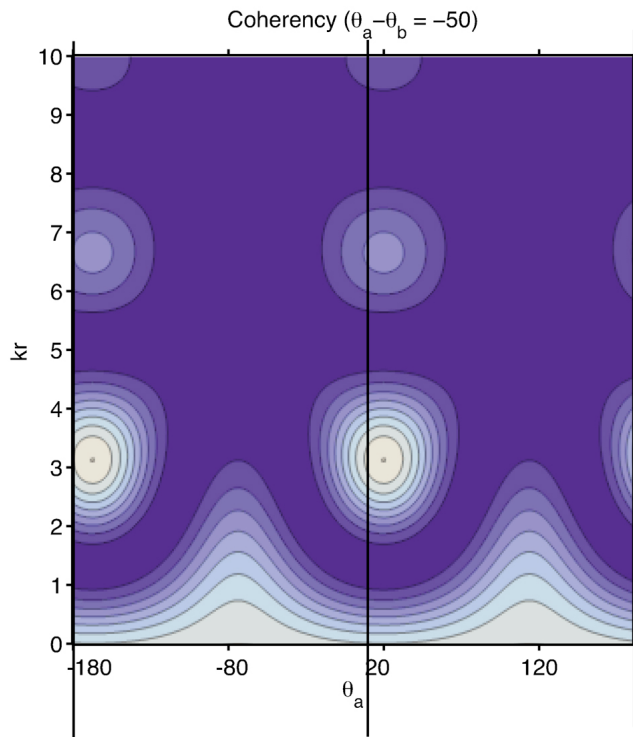
Figure 9. Coherency as a function of spin for a dual payload interferometer whose relative spin angle is −50 degrees. The x-axis, θ_a, is the orientation of payload a with respect to the inter-payload separation vector.
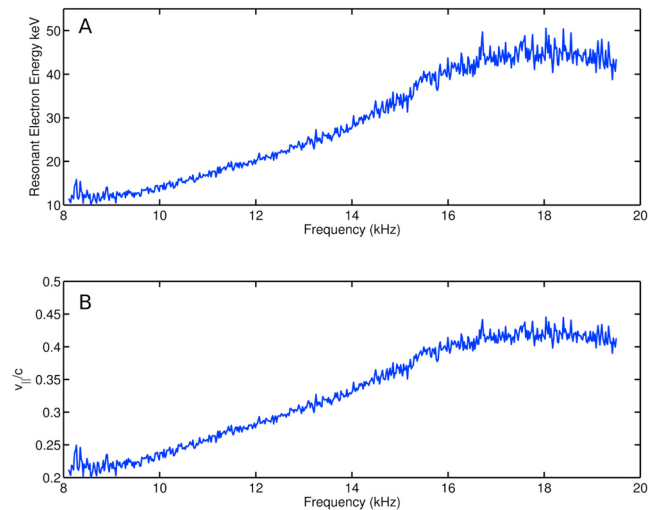
These two assumptions are verified experimentally in Figure 7, which shows near zero coherency where our model predicts it.

6. Conclusions

[36] Using a multiple payload sounding rocket mission we've successfully measured the parallel wavelength of
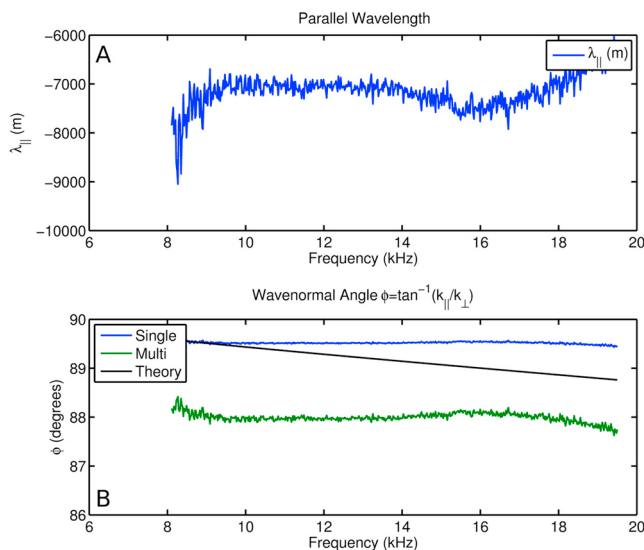
Figure 10. (a) The parallel wavelength deduced from inter-payload phase. (b) The wave-normal angle.

Figure 11. (a) The resonant electron energy. (b) Measured parallel phase velocity.

VLF hiss and bounded the perpendicular wavelength of VLF hiss. By calculating the interferometric response of two separated, arbitrarily oriented VLF wave antenna/recievers, we predicted nulls in the inter-payload coherency pattern. Observation of these nulls gave an upper bound estimate on the perpendicular wavelength of VLF hiss of ~345 m. Using a single payload interferometer, we confirmed previous perpendicular wavelength estimates of ~60 m. We also showed that the inter-payload phase spectrum was entirely a function of the inter-payload separation distance allowing for accurate estimation of the parallel wavelength of VLF hiss as a function of frequency of ~6–8 km. This constitutes one of very few parallel wavelength observations of space plasma waves. By combining our upper (lower) perpendicular wavelength estimates we computed lower (upper) estimates on observed wave normal angle which effectively bound the resonance cone angle predicted by cold plasma theory, verifying that VLF hiss falls on the whistler wave resonance cone.

[38] Robert Lysak thanks the reviewers for their assistance in evaluating this paper.

References

Bonnell, J. W. (1997), Identification of broadband ELF waves observed during transverse ion acceleration in the auroral ionosphere, PhD thesis, Cornell Univ., Ithaca, N. Y.
Dudok de Wit, T., V. V. Krasnosel'skikh, S. D. Bale, M. W. Dunlop, H. Lühr, S. J. Schwartz, and L. J. C. Woolliscroft (1995), Determination of dispersion relations in quasi-stationary plasma turbulence using dual satellite data, *Geophys. Res. Lett.*, *22*, 2653–2656, doi:10.1029/95GL02543.
Ergun, R. E., E. Klementis, C. W. Carlson, J. P. McFadden, and J. H. Clemmons (1991), Wavelength measurement of auroral hiss, *J. Geophys. Res.*, *96*(A12), 21,299–21,307, doi:10.1029/91JA01863.
Farley, D. T., H. M. Ierkic, and B. G. Fejer (1981), Radar interferometry: A new technique for studying plasma turbulence in the ionosphere, *J. Geophys. Res.*, *86*, 1467–1472, doi:10.1029/JA086iA03p01467.
Fisher, R. K., and R. W. Gould (1971), Resonance cones in the field pattern of a radio frequency probe in a warm anisotropic plasma, *Phys. Fluids*, *14*, 857–867, doi:10.1063/1.1693521.

Gurnett, D. A., and L. A. Frank (1972), VLF hiss and related plasma observations in the polar magnetosphere, *J. Geophys. Res.*, *77*, 172–190, doi:10.1029/JA077i001p00172.

Humphreys, T. E., M. L. Psiaki, E. M. Klatt, S. P. Powell, and P. M. Kintner (2005), Magnetometer-based attitude and rate estimation for spacecraft with wire booms, *J. Guidance Control Dyn.*, *28*, 584–593.

Kelley, M. C., and F. S. Mozer (1972), A satellite survey of vector electric fields in the ionosphere at frequencies of 10 to 500 hertz: 1. Isotropic, high-latitude electrostatic emissions, *J. Geophys. Res.*, *77*, 4158–4173, doi:10.1029/JA077i022p04158.

Kintner, P. M., J. Franz, P. Schuck, and E. Klatt (2000), Interferometric coherency determination of wavelength or what are broadband ELF waves?, *J. Geophys. Res.*, *105*, 21,237–21,250, doi:10.1029/1999JA000323.

LaBelle, J., and R. A. Treumann (2002), Auroral radio emissions, 1. Hisses, roars, and bursts, *Space Sci. Rev.*, *101*, 295–440.

Maggs, J. E. (1976), Coherent generation of VLF hiss, *J. Geophys. Res.*, *81*, 1707–1724, doi:10.1029/JA081i010p01707.

Pincon, J. L., and F. Lefeuvre (1992), The application of the generalized Capon method to the analysis of a turbulent field in space plasma—Experimental constraints, *J. Atmos. Terr. Phys.*, *54*, 1237–1247.

Powell, S. P., E. M. Klatt, and P. M. Kintner (2002), Plasma wave interferometry using GPS position and timing on a formation of three sub-orbital payloads, paper presented at 15th International Technical Meeting of the Satellite Division of the Institute of Navigation, Portland, Oreg.

Schuck, P. W., J. W. Bonnell, and P. M. Kintner (2003), A review of lower hybrid solitary structures, *IEEE Trans. Plasma Sci.*, *31*, 1125–1177, doi:10.1109/TPS.2003.822043.

Sonwalkar, V. S., and J. Harikumar (2000), An explanation of ground observations of auroral hiss: Role of density depletions and meter-scale irregularities, *J. Geophys. Res.*, *105*, 18,867–18,884, doi:10.1029/1999JA000302.

Ye, S., and J. LaBelle (2008), Ground based observations of low frequency auroral hiss fine structure, *J. Geophys. Res.*, *113*, A01313, doi:10.1029/2007JA012473.

E. T. Lundberg, MITRE Corporation, 202 Burlington Rd., Bedford, MA 01730, USA. (etl22@cornell.edu)

K. A. Lynch, Department of Physics, Dartmouth College, Hanover, NH 03755, USA.

S. P. Powell, Department of Electrical and Computer Engineering, Cornell University, Rhodes Hall 301, Ithaca, NY 14850, USA.